Supporting Information

A novel route to fabricate high-density graphene assemblies for high-volumetric-performance supercapacitors: Effect of cation pre-intercalation

Daoqing Liu, Zheng Jia*, Dianlong Wang

School of Chemical Engineering and Technology, Harbin Institute of Technology,

Harbin 150001, China

*Address correspondence to 13104059037@163.com.

Table of contents

1. Preparation of graphite oxide

Graphite oxide was prepared from natural graphite (Xinghe Co., Qingdao, China) according to a modified Hummers method, as we previously reported.[1] Briefly, 5 g natural graphite and 2.5 g $NaNO_3$ was added to 120 mL of concentrated H_2SO_4 under continuous stirring in an ice bath. Subsequently, 7.5g $KMnO_4$ was slowly added to the formed mixture, which was allowed to react under stirring at a temperature no more than 20℃ for 2 h. Then, the mixture was heated to 35℃ and kept reacting at that temperature for another 2 h. After that, the reactant mixture was slowly poured into 180 mL distilled water under violent stirring, followed by further reaction at 75℃ for 1 h. The mixture was then cooled to room temperature and poured into 1000 mL distilled water with 50 mL 30% H_2O_2. The obtained product was filtered and washed with 5 wt% HCl solution followed by distilled water. Finally, the filter cake was dried in air at 50℃ for 24 h to obtain the graphite oxide.

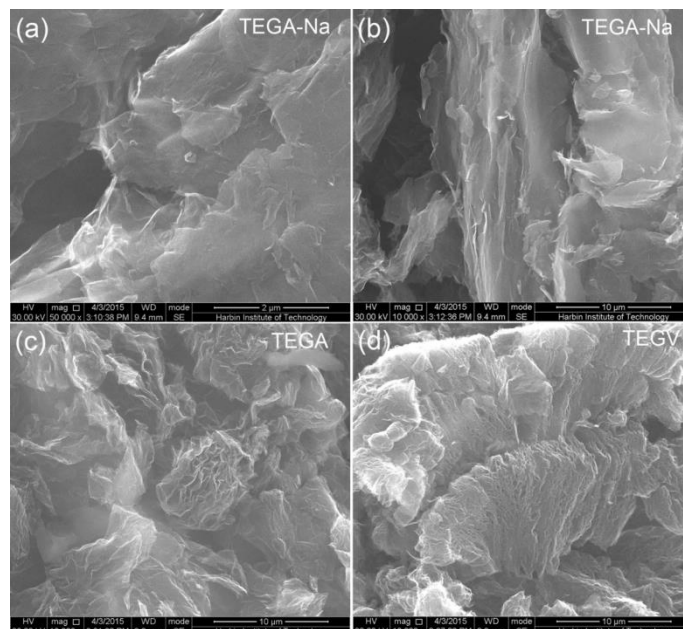# 2. Characterization of TEGA-Na and TEGA

Fig. S1 SEM images of (a and b) TEGA-Na, (c) TEGA and (d) TEGV.

As compared in Fig. S1, TEGA-Na shows a compact laminated structure of graphene layers without the large interlayer pores as observed in TEGA and TEGV, indicating its lowest thermal

expansion degree, and predicting its highest apparent density among these three graphene materials.
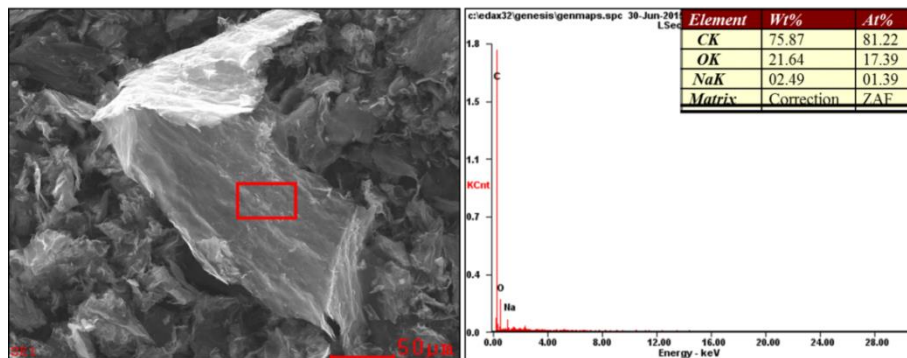

Fig. S2 EDX spectrum of TEGA-Na.

The EDX spectrum indicates that 1.39 at% Na is left in TEGA-Na.
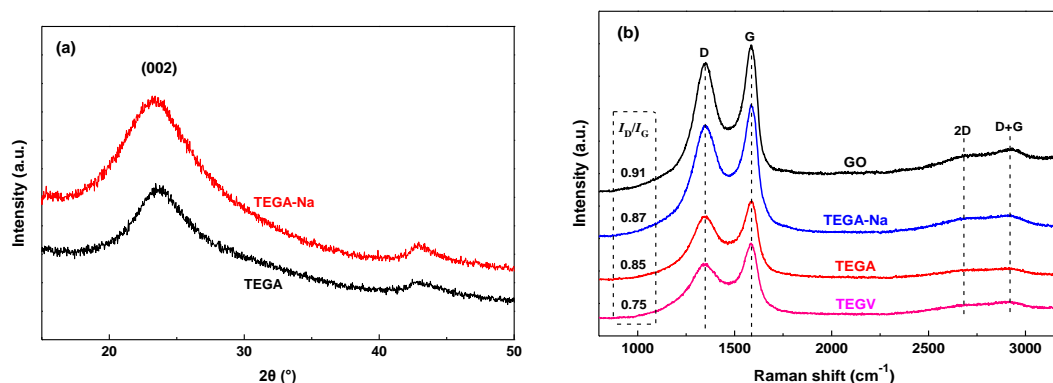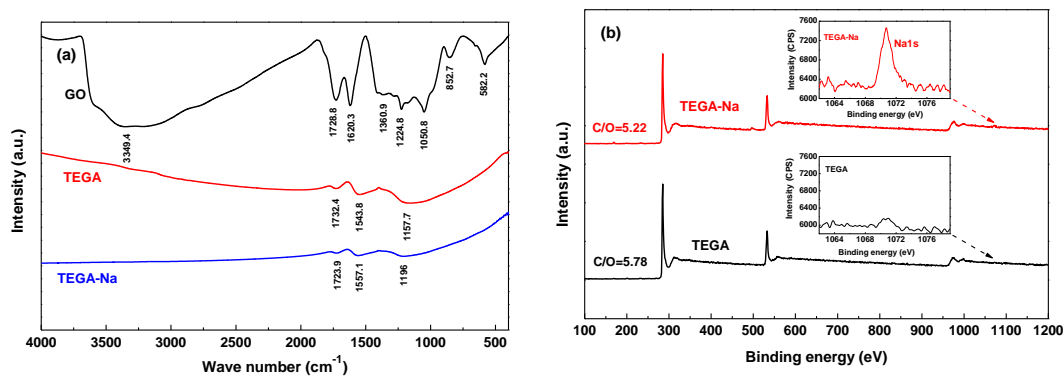

Fig. S3 (a) XRD patterns of TEGA-Na and TEGA. (b) Raman spectra of GO, TEGA-Na, TEGA and TEGV.
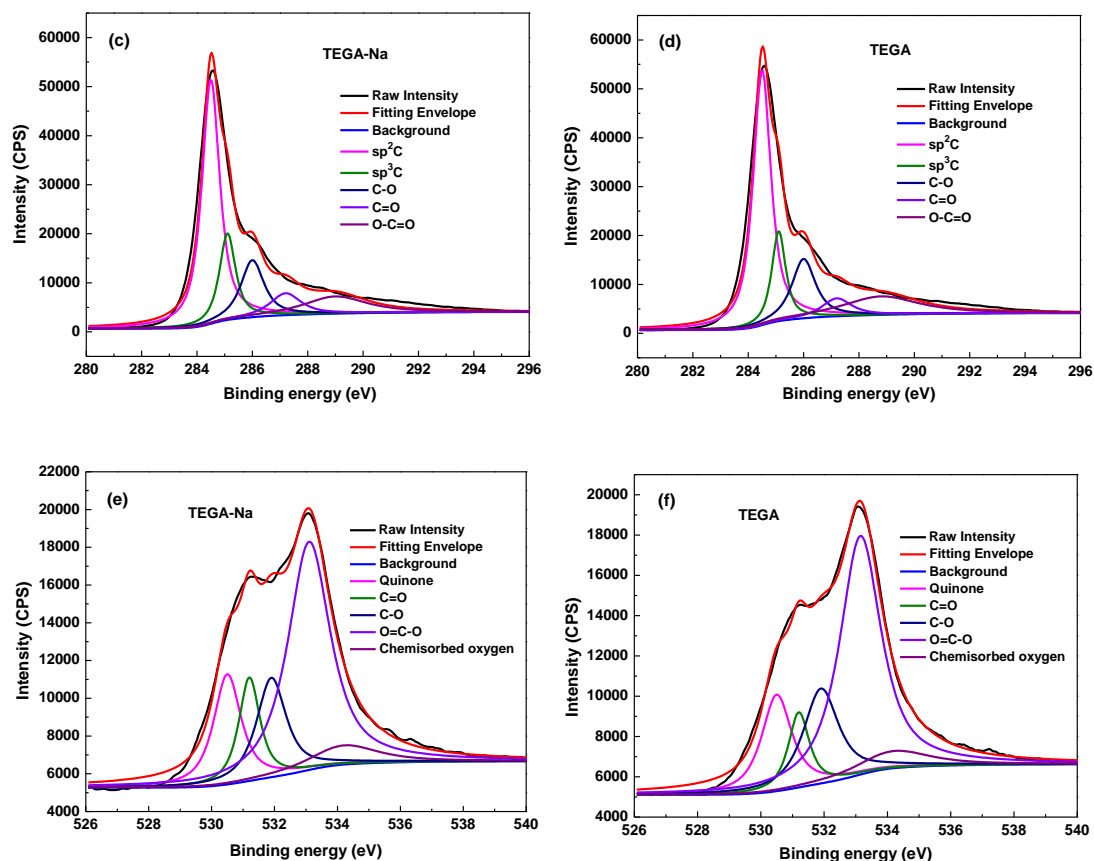
Fig. S4 (a) FTIR spectra of GO, TEGA and TEGA-Na. (b) XPS survey spectra of TEGA-Na and TEGA. Inset: the magnified Na 1S XPS spectra for TEGA-Na (top) and TEGA (bottom). C1s XPS spectra of (c) TEGA-Na and (d) TEGA. O1s XPS spectra of (e) TEGA-Na and (f) TEGA.

Table S1 Surface elemental concentrations and relative contents of functional groups derived from C1s XPS spectra of TEGA and TEGA-Na

Samples	Carbon (at.%)	Oxgen (at.%)	Na (at.%)	C1s fitting binding enrgy (eV; ralative percentage,%)				
				C=C(sp^2)	C-C(sp^3)	C-O	C=O	O-C=O
TEGA	85.19	14.81	-	284.5 (49.86)	285.1 (13.7)	286 (15.27)	287.2 (5.79)	288.8 (15.35)
TEGA-Na	83.47	15.98	0.55	284.5 (49.55)	285.1 (15.66)	286 (14.86)	287.2 (7.62)	289 (12.29)

Table S2 Relative contents of functional groups derived from O1s XPS spectra of TEGA and TEGA-Na

Samples	O1s fitting binding enrgy (eV; ralative percentage,%)				
	Quinone	C=O	C-O	O=C-O	Chemisorbed oxygen
TEGA	530.5 (15.39)	531.2 (8.34)	531.9 (17.71)	533.1 (51.97)	534.2 (6.56)
TEGA-Na	530.5 (15.85)	531.2 (11.48)	531.9 (15.43)	533.1 (50.33)	534.2 (6.9)

5

3. Supercapacitive performances of TEGA-Na and TEGA in 30 wt% KOH aqueous electrolyte
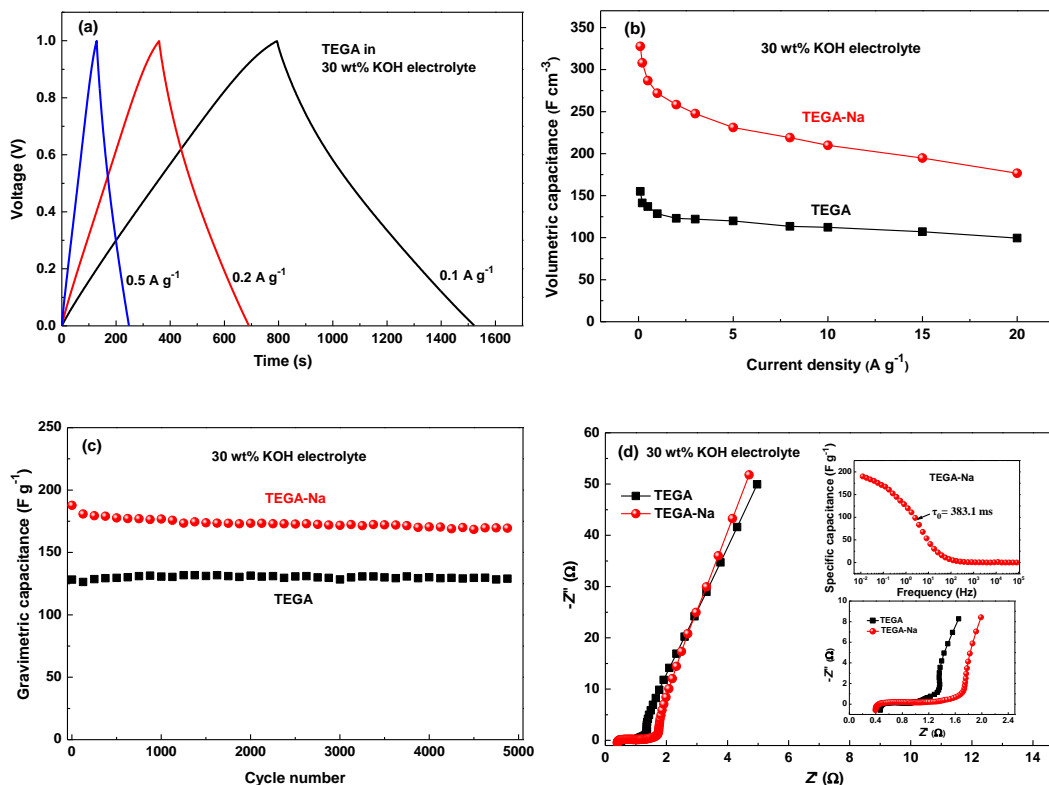
Fig. S5 Supercapacitive performances of TEGA-Na and TEGA in a symmetric two-electrode system in 30 wt% KOH aqueous electrolyte. (a) Galvanostatic charge/discharge curves of TEGA at different current densities. (b) Comparison of volumetric capacitance values of TEGA-Na and TEGA at different current densities. (c) Cycling stability of the gravimetric capacitance values of TEGA-Na and TEGA at a current density of 1 A g^{-1}. (d) Nyquist plots of TEGA-Na and TEGA, inset: the magnified high-frequency region of the Nyquist plots (bottom) and the corresponding frequency response curves of gravimetric capacitance of TEGA-Na (top).

4. Supercapacitive performances of TEGA-Na and TEGA in 1 mol L^{-1} Na$_2$SO$_4$ aqueous electrolyte
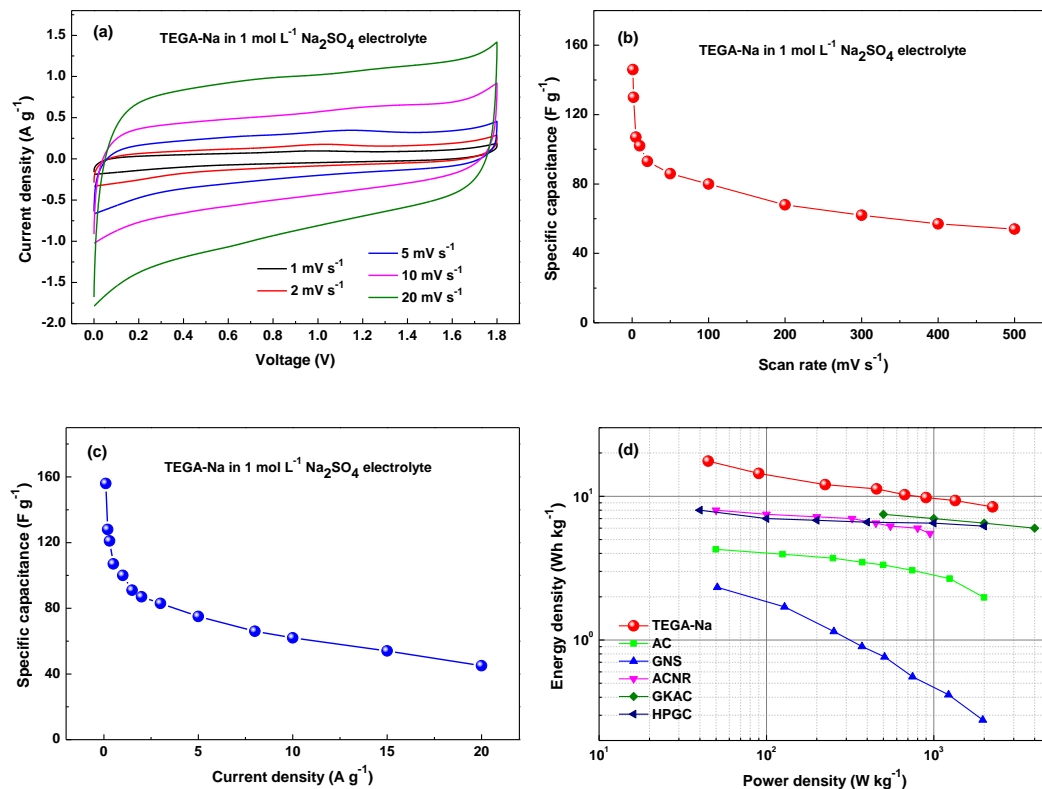
Fig. S6 Supercapacitive performances of TEGA-Na in a symmetric two-electrode system in 1 mol L^{-1} Na$_2$SO$_4$ aqueous electrolyte within a voltage range of 0-1.8 V. (a) CV curves at low scan rates. (b) Gravimetric capacitance values at different scan rates. (c) Gravimetric capacitance values at different current densities. (d) Comparison of the gravimetric Ragone plot in aqueous electrolytes of TEGA-Na with some representative carbon materials, including AC and GNS,[1] ACNR,[2] GKAC[3] and HPGC.[4]

5. Supercapacitive performances of TEGA-Na and TEGA in 1 mol L⁻¹ Et₄NBF₄/AN organic electrolyte
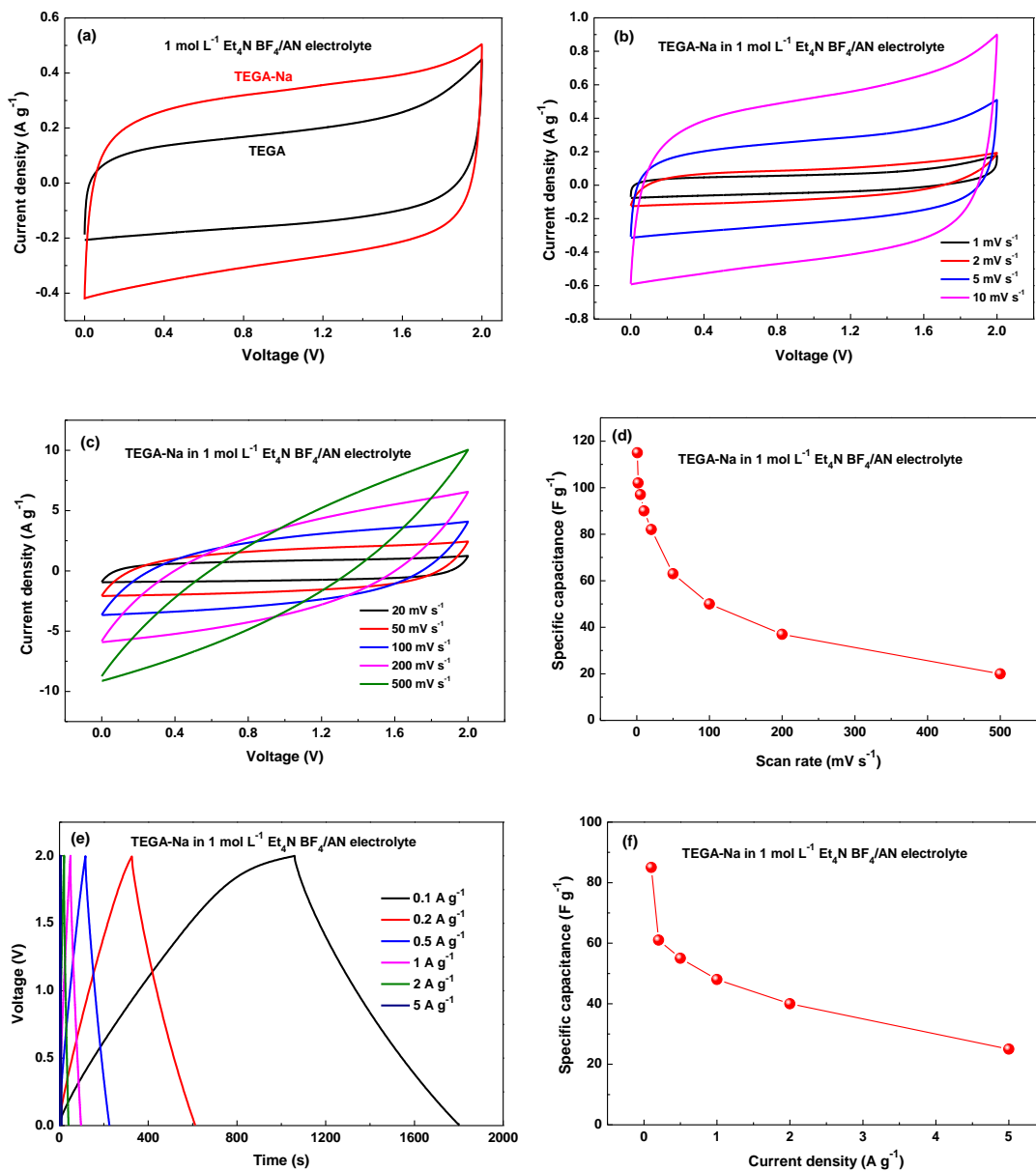
Fig. S7 Supercapacitive performance of TEGA-Na and TEGA in a symmetric two-electrode system in 1 mol L^{-1} Et$_4$NBF$_4$/AN organic electrolyte. (a) CV curves of TEGA-Na and TEGA at a scan rate of 10 mV s^{-1}. CV curves of TEGA-Na at (b) low and (c) high scan rates. (d) Gravimetric capacitances of TEGA-Na at different scan rates. (e) Galvanostatic charge/discharge curves of TEGA-Na at different current densities. (f) Gravimetric capacitances of TEGA-Na at different current densities.

6. Characterization of TEGV, TEGV-H and TEGV-K

Fig. S8 Digital photos of GO suspension (a) before and (b) after the addition of KCl or HCl and (c) the powders of TEGV-K (0.2 g), TEGV-H (0.2 g) and TEGV (0.1 g). SEM imagess of (d) TEGV, (e) TEGV-H and (f-g) TEGV-K.

Fig. S9 (a) XRD patterns of TEGV, TEGV-H and TEGV-K. (b) N_2 adsorption/desorption isotherms and the corresponding pore size distribution (inset) of TEGV-H and TEGV-K. (c) CO_2 adsorption isotherms and (d) the corresponding pore size distribution of TEGV, TEGV-H and TEGV-K.

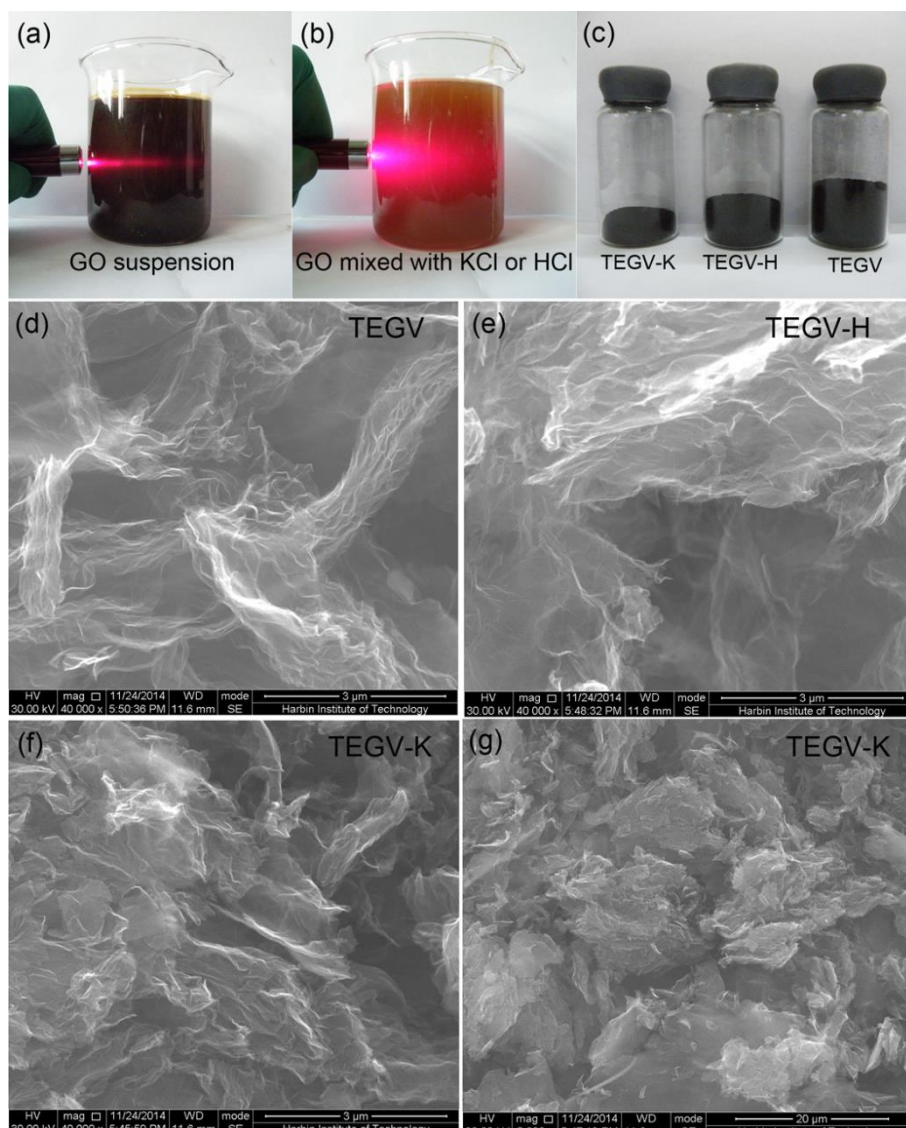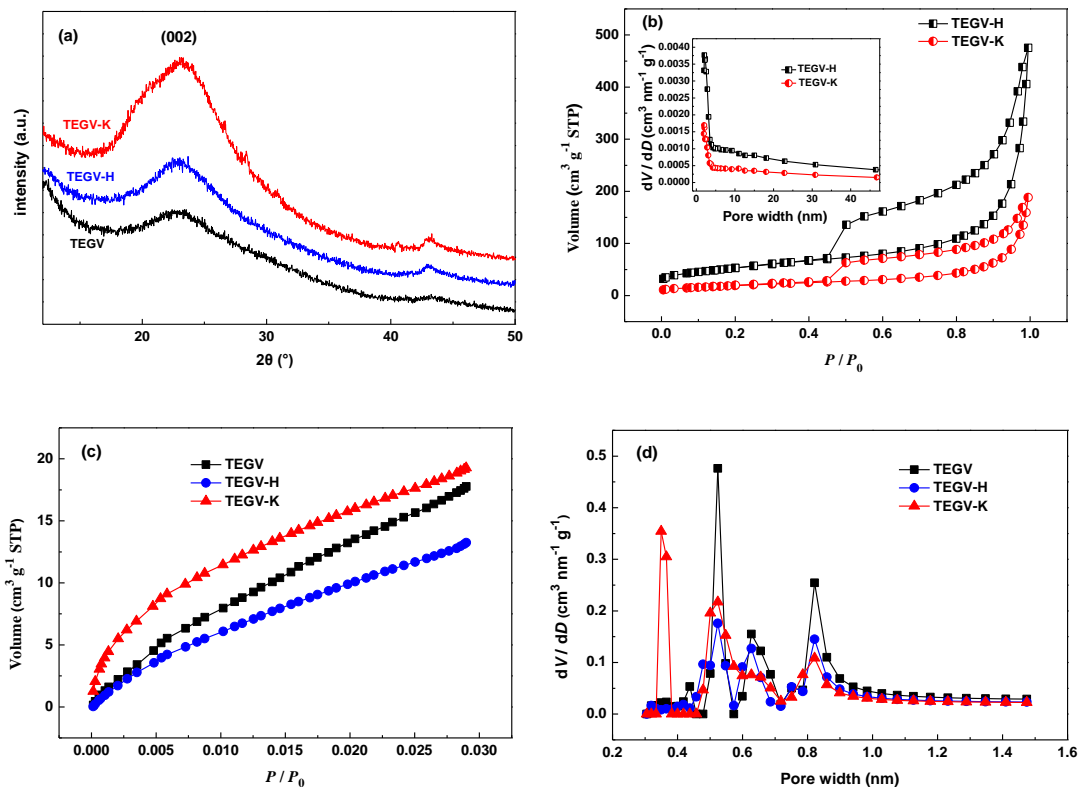Table S3. Porosity parameters and densities of TEGV, TEGV-H and TEGV-K

Sample	S_{N_2} [a]	V_{N_2} [b]	S_{CO_2} [c]	V_{CO_2} [d]	S_{Total} [e]	V_{Total} [f]	ρ_1 [g]	ρ_2 [h]
	[$m^2\ g^{-1}$]	[$cm^3\ g^{-1}$]	[$m^2\ g^{-1}$]	[$cm^3\ g^{-1}$]	[$m^2\ g^{-1}$]	[$cm^3\ g^{-1}$]	[$g\ cm^{-3}$]	[$g\ cm^{-3}$]
TEGV	271.01	0.6797	192.17	0.069	463.18	0.7487	0.48	0.80
TEGV-H	189.07	0.4373	142.58	0.051	331.65	0.4883	0.82	1.01
TEGV-K	69.37	0.1814	199.11	0.061	268.48	0.2424	1.17	1.35

[a] SSA calculated with BET method from the N_2 adsorption isotherm;

[b] Single point adsorption pore volume at $P/P_0 = 0.97$ from the N_2 adsorption isotherm;

[c] SSA calculated with DFT method from the CO_2 adsorption isotherm;

[d] Pore volume calculated with DFT method from the CO_2 adsorption isotherm;

[e] The sum of BET SSA derived from the N_2 isotherm and DFT SSA derived from the CO_2 isotherm, i.e., $S_{Total} = S_{N2} + S_{CO2}$;

[f] The sum of pore volume derived from the N_2 isotherm and that from the CO_2 isotherm, i.e., $V_{Total} = V_{N2} + V_{CO2}$;

[g] ρ_1 is the electrode sheet density, obtained by the compression method based on the total mass of electrode materials, including the graphene material, acetylene black and PTFE;

[h] ρ_2 is the apparent density of the graphene sample, calculated by $\rho = \left\{ V_{Total} + {1}/{\rho_{Carbon}} \right\}^{-1}$, where $\rho_{Carbon} = 2$ $g\ cm^{-3}$.

From the above characterization results (the SEM images in Fig. S8, adsorption results in Fig. S9 and Table S3), we can speculate that the differences of TEGV, TEGV-H and TEGV-K in micromorphology, porosity structure and apparent density should result from their various precursors for thermal expansion.

As to TEGV-H, the HCl molecules incorporated in the GO aggregate will volatile during the desiccation procedure, thus the thermal expansion precursor of TEGV-H is the coagulated GO aggregate without HCl residues. The lower SSA and higher density of TEGV-H compared with TEGV indicates that the graphene layers in the GO aggregate coagulated by HCl stack not as firmly as those in the original graphite oxide.

As for TEGV-K, the thermal expansion precursor is the coagulated GO aggregate with intercalated K^+ ions. Therefore, the further lower SSA and higher density of TEGV-K compared with TEGV-H may imply that the intercalation of K^+ ions makes GO layers stack more loosely so that the thermal expansion degree is further lowered.

7. Supercapacitive performances of TEGV, TEGV-H and TEGV-K in 30 wt% KOH aqueous electrolyte
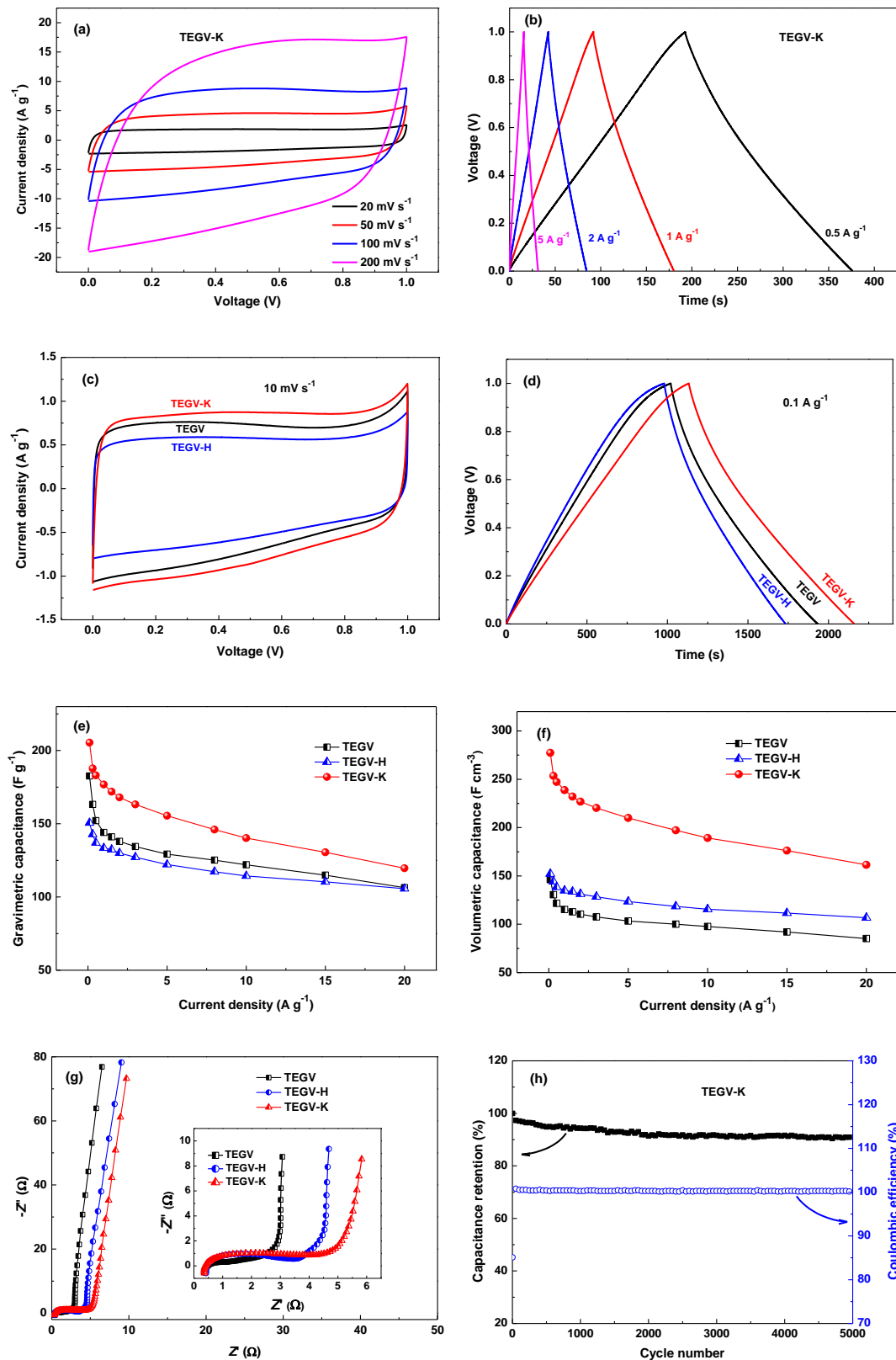
Fig. S10 Supercapacitive performance of TEGV, TEGV-H and TEGV-K in a symmetric two-electrode system in 30 wt% KOH aqueous electrolyte. (a) CV curves of TEGV-K at different scan rates. (b) Galvanostatic charge/discharge curves of TEGV-K at various current densities. (c) CV curves of TEGV, TEGV-H and TEGV-K at a scan rate of 10 mV s^{-1}. (d) Galvanostatic charge/discharge curves of TEGV, TEGV-H and TEGV-K at a current density of 0.1 A g^{-1}. (e) Gravimetric and (f) volumetric specific capacitances of TEGV, TEGV-H and TEGV-K at different current densities. (g) Nyquist plots of TEGV, TEGV-H and TEGV-K. Inset: the magnified high frequency region of the Nyquist plots. (h) Cycling performance curves of TEGV-K.

8. Comparison of the gravimetric and volumetric capacitances in aqueous electrolytes of different carbon materials

Table S4 Comparison of the gravimetric and volumetric capacitances in aqueous electrolytes of different carbon materials.

Materials	C_g [F g^{-1}]	C_V [F cm^{-3}]	Electrolyte	Test device	Ref.
KOH reduced graphene (KrGO)	322 (1mV s^{-1})	502	1M H$_2$SO$_4$	**Three-electrode**	[1]
High density porous graphene macroform (HPGM)	260	410	6M KOH	**Three-electrode**	[5]
High surface-area graphite	205	180	6M KOH	**Three-electrode**	[6]
Activeted mesoporous carbons	223 (1 mV s^{-1})	54	6M KOH	**Three-electrode**	[7]
Activated porous carbons (CS15A6)	223 (2 mV s^{-1})	54	6M KOH	**Three-electrode**	[8]
Carbon Xerogel Microspheres (CXAη-30)	251 (0.5 mV s^{-1})	166	1M H$_2$SO$_4$	**Three-electrode**	[9]
Cu-doped carbon xerogel microspheres (CXCu-30)	174 (1A g^{-1})	146	1M H$_2$SO$_4$	**Three-electrode**	[10]
Activated Cu-doped carbon aerogel (CReCu20)	192 (0.125 A g^{-1})	98	1M H$_2$SO$_4$	**Three-electrode**	[11]
Monolithic porous carbon	145 (1 mV s^{-1})	125	1M H$_2$SO	**Three-electrode**	[12]
Monodisperse carbon nanospheres (CNSs-6)	328 (5 mV s^{-1})	383	6M KOH	**Three-electrode**	[13]
Reduced graphene oxide by urea	255 (0.5 A g^{-1})	196	6M KOH	**Three-electrode**	[14]
S-doped carbon–graphene composites	109 (50 mA cm^{-2})	65	6M KOH	**Three-electrode**	[15]
Functionalized graphene (FGN300)	456 (0.5 A g^{-1})	470	6M KOH	**Three-electrode**	[16]
Functional pillared graphene frameworks (FPGF-200)	353 (2 mV s^{-1})	400	6M KOH	**Three-electrode**	[17]
Liquid-mediated graphene (EM-CCG film)	191.7 (0.1 A g^{-1})	255.5	1M H$_2$SO$_4$	**Two-electrode**	[18]
High density porous graphene macroform (HPGM)	238 (0.1 A g^{-1})	376	6M KOH	**Two-electrode**	[5]
KOH reduced graphene (KrGO)	205 (0.2 A g^{-1})	314	1M H$_2$SO$_4$	**Two-electrode**	[1]
Seaweeds derived carbon (ALG-C)	198 (2 mV s^{-1})	180	1M H$_2$SO$_4$	**Two-electrode**	[19]
Seaweeds derived carbon (LN600)	264 (2 mV s^{-1})	208	1M H$_2$SO$_4$	**Two-electrode**	[20]
High density reduced graphene oxide (RGO-HD)	182 (1 A g^{-1})	255	6M KOH	**Two-electrode**	[21]
Holey graphene framework (HGF)	310 (1 A g^{-1})	220	6M KOH	**Two-electrode**	[22]
Ordered mesoporous carbon nanospheres (OMCNS)	173 (1 mA cm^{-2})	107	6M KOH	**Two-electrode**	[23]
Ultramicroporous carbon	264 (0.05 A g^{-1})	218	6M KOH	**Two-electrode**	[24]
Nitrogen-Enriched Nonporous Carbon	198 (0.05 A g^{-1})	280	6M KOH	**Two-electrode**	[25]
	115 (0.05 A g^{-1})	152	1M H$_2$SO$_4$		

Dense carbon monoliths (CM)	292 (1 mA cm^{-2})	342	2M H$_2$SO	**Two-electrode**	[26]
Activated carbon	339 (50 mA g^{-1})	171	6M KOH	**Two-electrode**	[27]
Carbide-derived carbons (CDCs)	200 (1 mA cm^{-2})	90	2M H$_2$SO$_4$	**Two-electrode**	[28]
N-doped carbon microspheres (N-CSA-600)	310 (0.1 A g^{-1})	290	1M H$_2$SO$_4$	**Two-electrode**	[29]
Porous wood carbon monolith (m-WCM)	234 (10 mA cm^{-2})	36	2M KOH	**Two-electrode**	[30]
Activated MCMB	~300 (0.2 A g^{-1})	~160	6M KOH	**Two-electrode**	[31]
Single-Walled Carbon Nanohorns (HT1273K)	122 (5 mA cm^{-2})	47	30 wt % H$_2$SO$_4$	**Two-electrode**	[32]
Porous layer-stacking carbon (PGC)	374 (0.5A g^{-1})	360	6M KOH	**Two-electrode**	[33]
TEGA	145 (0.1 A g^{-1})	153	30 wt % KOH	**Two-electrode**	This work
TEGA-Na	**217 (0.1 A g^{-1})**	**328**	**30 wt % KOH**	**Two-electrode**	**This work**

References

1. D. Q. Liu, Z. Jia, J. X. Zhu and D. L. Wang, *Journal of Materials Chemistry A*, 2015, **3**, 12653-12662.

2. P. Ramakrishnan, S.-G. Park and S. Shanmugam, *Journal of Materials Chemistry A*, 2015, **3**, 16242-16250.

3. S. Yu, Y. Li and N. Pan, *Rsc Advances*, 2014, **4**, 48758-48764.

4. D. W. Wang, F. Li, M. Liu, G. Q. Lu and H. M. Cheng, *Angewandte Chemie-International Edition*, 2009, **48**, 1525-1525.

5. Y. Tao, X. Xie, W. Lv, D.-M. Tang, D. Kong, Z. Huang, H. Nishihara, T. Ishii, B. Li, D. Golberg, F. Kang, T. Kyotani and Q.-H. Yang, *Sci Rep-Uk*, 2013, **3**, 2975.

6. H. Q. Li, Y. G. Wang, C. X. Wang and Y. Y. Xia, *J Power Sources*, 2008, **185**, 1557-1562.

7. K. Xia, Q. Gao, J. Jiang and J. Hu, *Carbon*, 2008, **46**, 1718-1726.

8. K. S. Xia, Q. M. Gao, J. H. Jiang and J. Hu, *Carbon*, 2008, **46**, 1718-1726.

9. Z. Zapata-Benabithe, F. Carrasco-Marín, J. de Vicente and C. Moreno-Castilla, *Langmuir*, 2013, **29**, 6166-6173.

10. Z. Zapata-Benabithe, J. de Vicente, F. Carrasco-Marín and C. Moreno-Castilla, *Carbon*, 2013, **55**, 260-268.

11. Z. Zapata-Benabithe, F. Carrasco-Marin and C. Moreno-Castilla, *Mater Chem Phys*, 2013, **138**, 870-876.

12. M. M. Bruno, N. G. Cotella, M. C. Miras, T. Koch, S. Seidler and C. Barbero, *Colloid Surface A*, 2010, **358**, 13-20.

13. D. S. Yuan, J. X. Chen, J. H. Zeng and S. X. Tan, *Electrochem Commun*, 2008, **10**, 1067-1070.

14. Z. B. Lei, L. Lu and X. S. Zhao, *Energ Environ Sci*, 2012, **5**, 6391-6399.

15. M. Seredych and T. J. Bandosz, *J Mater Chem A*, 2013, **1**, 11717-11727.

16. J. Yan, Q. Wang, T. Wei, L. L. Jiang, M. L. Zhang, X. Y. Jing and Z. J. Fan, *Acs Nano*, 2014, **8**, 4720-4729.

17. L. L. Jiang, L. Z. Sheng, C. L. Long, T. Wei and Z. J. Fan, *Adv Energy Mater*, 2015, **5**, 1500771.

18. X. Yang, C. Cheng, Y. Wang, L. Qiu and D. Li, *Science*, 2013, **341**, 534-537.

19. E. Raymundo-Pinero, F. Leroux and F. Beguin, *Adv Mater*, 2006, **18**, 1877-1882.

20. E. Raymundo-Pinero, M. Cadek and F. Beguin, *Adv Funct Mater*, 2009, **19**, 1032-1039.

21. Y. Li and D. Zhao, *Chem Commun*, 2015, **51**, 5598-5601.

22. Y. X. Xu, Z. Y. Lin, X. Zhong, X. Q. Huang, N. O. Weiss, Y. Huang and X. F. Duan, *Nature Communications*, 2014, **5**, 4554.

23. X. L. Yu, J. G. Wang, Z. H. Huang, W. C. Shen and F. Y. Kang, *Electrochem Commun*, 2013, **36**, 66-70.

24. B. Xu, S. S. Hou, H. Duan, G. P. Cao, M. Chu and Y. S. Yang, *J. Power Sources*, 2013, **228**, 193-197.

25. D. Hulicova-Jurcakova, M. Kodama, S. Shiraishi, H. Hatori, Z. H. Zhu and G. Q. Lu, *Adv Funct Mater*, 2009, **19**, 1800-1809.

26. M. Kunowsky, A. Garcia-Gomez, V. Barranco, J. M. Rojo, J. Ibanez, J. D. Carruthers and A. Linares-Solano, *Carbon*, 2014, **68**, 553-562.

27. B. Xu, Y. F. Chen, G. Wei, G. P. Cao, H. Zhang and Y. S. Yang, *Mater Chem Phys*, 2010, **124**, 504-509.

28. J. A. Fernandez, M. Arulepp, J. Leis, F. Stoeckli and T. A. Centeno, *Electrochim Acta*, 2008, **53**, 7111-7116.

29. G. A. Ferrero, A. B. Fuertes and M. Sevilla, *Electrochim. Acta*, 2015, **168**, 320-329.

30. M. C. Liu, L. B. Kong, P. Zhang, Y. C. Luo and L. Kang, *Electrochim Acta*, 2012, **60**, 443-448.

31. K. Torchala, K. Kierzek and J. Machnikowski, *Electrochim Acta*, 2012, **86**, 260-267.

32. H. J. Jung, Y. J. Kim, J. H. Han, M. Yudasaka, S. Iijima, H. Kanoh, Y. A. Kim, K. Kaneko and C. M. Yang, *J Phys Chem C*, 2013, **117**, 25877-25883.

33. C. Long, X. Chen, L. Jiang, L. Zhi and Z. Fan, *Nano Energy*, 2015, **12**, 141-151.